Self-Assembled Minimalist Multifunctional Theranostic Nanoplatform for Magnetic Resonance Imaging-Guided Tumor Photodynamic Therapy

Zhang, Han; Liu, Kai; Li, Shukun; Xin, Xia; Yuan, Shiling; Ma, Guanghui; Yan, Xuehai

Published in:
Acs Nano

DOI:
10.1021/acsnano.8b03529

Publication date:
2018

ACS NANO
Cite This: ACS Nano 2018, 12, 8266–8276
www.acsnano.org

ARTICLE

Self-Assembled Minimalist Multifunctional Theranostic Nanoplatform for Magnetic Resonance Imaging-Guided Tumor Photodynamic Therapy

Han Zhang,[†,‡] Kai Liu,[‡,§,¶] Shukun Li,[‡,§] Xia Xin,[*,†,⊥] Shiling Yuan,[*,†] Guanghui Ma,[‡] and Xuehai Yan[*,‡,§,∥]

[†]Key Lab for Colloid and Interface Chemistry of Education Ministry, School of Chemistry and Chemical Engineering, Shandong University, Jinan 250100, P.R. China

[‡]State Key Laboratory of Biochemical Engineering, Institute of Process Engineering, Chinese Academy of Sciences, Beijing 100190, P.R. China

[§]University of Chinese Academy of Sciences, Beijing 100049, P.R. China

[∥]Center for Mesoscience, Institute of Process Engineering, Chinese Academy of Sciences, Beijing 100190, P.R. China

[⊥]National Engineering Technology Research Center for Colloidal Materials, Shandong University, Jinan 250100, P.R. China

Supporting Information

ABSTRACT: **Minimalist multifunctional platforms for delivering diagnostic and therapeutic agents effectively and safely into tumor sites are highly desired in nanomedicine. Herein, we describe the fabrication of a supramolecular nanoplatform *via* the amphiphilic amino acid (9-fluorenylmethyloxycarbonyl-L-leucine, Fmoc-L-L)-modulated self-assembly of a magnetic resonance imaging (MRI) contrast agent (ionic manganese, Mn^{2+}) and photosensitive drug (chlorin e6, Ce6). Coordination drives the coassembly of Fmoc-L-L and Mn^{2+} to generate a nanoscale supramolecular network to adaptively encapsulate Ce6. The obtained biometal−organic nanoparticles exhibit a high drug loading capability, inherent good biocompatibility, robust stability, and smart disassembly in response to glutathione (GSH). The cooperative assembly of the multiple components is synchronously dynamic in nature and enables enhanced photodynamic therapy (PDT) to damage tumor cells and tissue by efficiently delivering the photosensitizer and improving the reductive tumor microenvironment *via* the competitive coordination of GSH with Mn^{2+}. The antitumor effect can also be monitored and evaluated *in vivo* by MRI through the long-term intracellular biochelation of Mn^{2+}. Therefore, this work presents a one-pot and robust method for the self-assembly of a multifunctional theranostic nanoplatform capable of MRI-guided PDT starting from minimalist biological building blocks.**

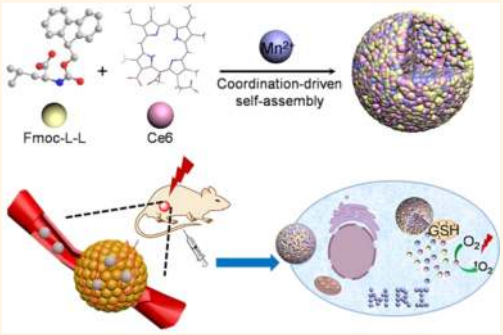

KEYWORDS: *self-assembly, amino acid, nanoplatform, magnetic resonance imaging, photodynamic therapy*

The controlled integration of medical diagnostics, drug delivery, and efficient therapy into a single nanoplatform system has emerged as a promising tool in personalized medicine.[1−5] Imaging-guided systems are particularly useful for treating tumors (*e.g.*, phototherapy) and easily evaluating the response to therapy, thus providing important post-treatment information regarding solid tumors.[6−10] Magnetic resonance imaging (MRI) can detect the anatomical information on biological tissues with high resolution and excellent depth in real time and *in vivo*.[11−13] MRI contrast agents (*e.g.*, iron oxide and manganese oxide) have been widely used to construct theranostic platforms.[14,15] Although promising, inorganic nanocarriers present inherent concerns regarding their long-term safety, low drug loading efficiency (<5 wt %), and/or the rapid release of the proportion of drug molecules that are simply adsorbed (or anchored) to their surface.[16−18] Additional efforts have typically been focused on approaches for integrating both therapeutic molecules and paramagnetic ions into lipid- and polymer-based nanostructures by attachment or encapsulation.[19−21] However, tedious

Received: May 10, 2018
Accepted: August 9, 2018
Published: August 9, 2018

DOI: 10.1021/acsnano.8b03529
ACS Nano 2018, 12, 8266–8276

Scheme 1. Schematic Illustration of the Fabrication Process of FMCNPs *via* Coordination-Driven Self-Assembly and Their Responsive Disassembly for MRI-Guided PDT

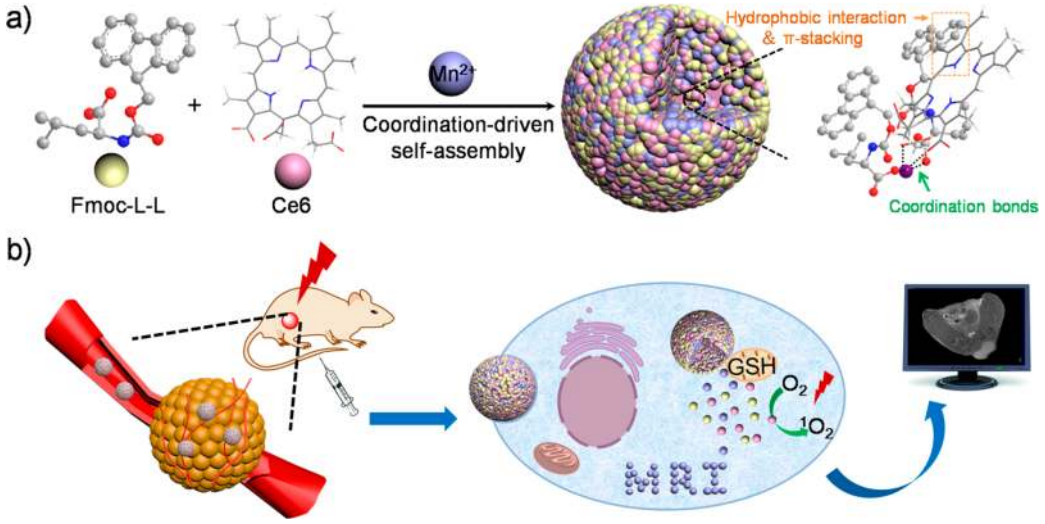

synthesis and multistep integration methods are inevitably required for these systems, which limits their availability and applicability. Therefore, developing a facile strategy for fabricating platforms for the co-delivery of therapeutic and imaging agents for theranostic applications remains challenging.

Photodynamic therapy (PDT) is a minimally invasive therapeutic approach for the treatment skin cancer and subcutaneous tumors.[22] In PDT, the irradiation of photosensitizers produces many reactive oxygen species (ROS) to kill cancer cells.[23] The stimulus-triggered release of therapeutic and imaging agents (*e.g.*, photosensitizers and MRI contrast agents) into target pathological tissues and cells is highly desirable for enhanced theranostic efficacy.[24−28] With the hypoxia in tumor tissue, the intracellular levels of glutathione (GSH) in cancer cells are much higher (100−1000-fold) than those in normal cells.[29] This characteristic has inspired the introduction of redox-sensitive sites (*e.g.*, disulfide) into polymeric drug delivery systems to enhance the exposure of cancer cells to therapeutic molecules,[30] which heavily relies on skillful polymer synthesis.[31] Although high concentrations of GSH facilitate the development of tumor-responsive theranostic systems, they are detrimental to PDT as they reduce the generated ROS.[32,33] Therefore, to improve the therapeutic efficacy of PDT, the tumor-responsive production of ROS and the simultaneous elimination of intracellular GSH is of great value. Recently, attention has been directed toward reducing GSH levels by employing redox-active components (*e.g.*, metal ions and metallic oxide) and metal−organic frameworks *via* chemical consumption or physical adsorption, respectively.[34−36] To the best of our knowledge, the rational design of nanomaterials that integrate both of these ideal functions (*i.e.*, GSH-responsive release of photosensitizers accompanied by reduced active GSH level) has rarely been reported.[34]

Molecular self-assembly that leverages cooperative coassembly is becoming a popular strategy in the design and synthesis of multicomponent functional materials.[37−42] Coordination-driven self-assembly is an elegant "bottom-up" strategy for the construction of biohybrid architectures.[43−47] Metal−organic matrixes can control guest encapsulation and release, but porosity control can be challenging.[48] A simpler approach is to employ the adaptive self-assembly of subunits to form amorphous coordination-bonding networks that are capable of being adjusted based on the physicochemical properties (*e.g.*, charge and shape) of the guest molecules.[49,50] Due to the dynamic nature and excellent stimuli-responsiveness of noncovalent bonds (*e.g.*, metal−ligand coordination bonds and $\pi-\pi$ stacking), assembled nanomedicines exhibiting properties greater than the total properties of the individual components have great promise for theranostic applications in cancer.[51,52] Nevertheless, the dynamic process can be dramatically slowed to a kinetically trapped state through crystallization, glass transition, or gelation in high molecular weight systems.[53] Hence, small-molecule-mediated self-assembly without phase changes should alleviate these issues. Amino acids and their derivatives (*e.g.*, Fmoc-modified amino acids) are suitable building blocks with structural diversity, low cost, facile production, and inherent biocompatibility.[54−56] Amino-acid-coordinated self-assembly can generate various structures but is generally limited to ordered molecular networks due to the hydrogen bonding involved,[56] which may be incompatible with adaptive encapsulation for high loading.

Herein, we describe the development of a multicomponent nanoplatform based on the amphiphilic amino-acid-coordinated self-assembly of metal ions with the simultaneous encapsulation of photosensitive drugs (Scheme 1). Amphiphilic 9-fluorenylmethyloxycarbonyl-L-leucine (Fmoc-L-L) (Figure S1) coordinates with Mn^{2+}, a biocompatible T_1 contrast agent with a high spin number,[57] forming Fmoc-L-L/Mn^{2+} nanoparticles (FMNPs); during this process, chlorin e6 (Ce6) (Figure S1) molecules are integrated into the coordination networks to generate Fmoc-L-L/Mn^{2+}/Ce6 nanoparticles (FMCNPs) *via* the synergy of coordination, hydrophobic, and $\pi-\pi$ stacking interactions. Owing to the potent coordination of Mn^{2+} and Fmoc-L-L and Ce6, high drug loading (up to 36 wt %) can be obtained. The drugs and metal ions loaded in the FMCNPs are stable in a simulated physiological environment due to the multiple noncovalent interactions. The dynamic nature of the metal−ligand bonds is retained in the FMCNPs, which makes them labile to GSH, analogous to the tumor microenvironment, resulting in the responsive release of Ce6 and Mn^{2+} (Scheme 1). Meanwhile,

DOI: 10.1021/acsnano.8b03529
ACS Nano 2018, 12, 8266−8276

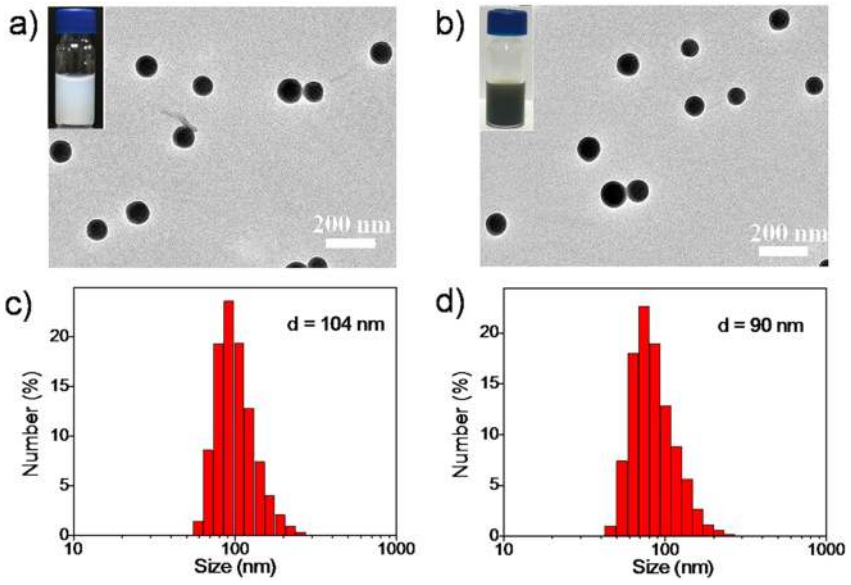

Figure 1. TEM images of assembled (a) FMNPs and (b) FMCNPs. The insets are corresponding photographs of the samples. Size distribution of (c) FMNPs and (d) FMCNPs as measured by DLS.

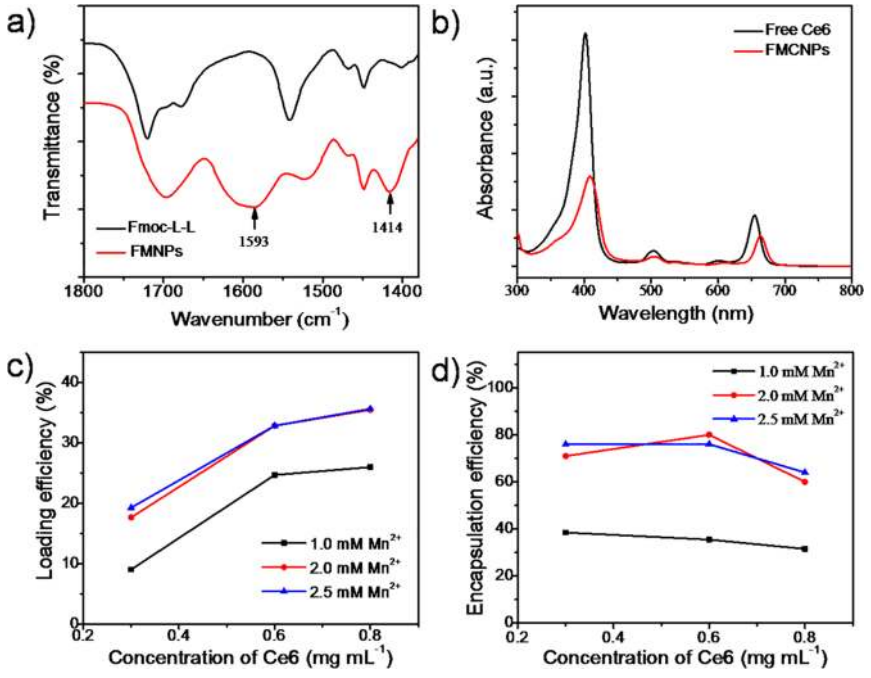

Figure 2. (a) FTIR spectra of Fmoc-L-L and FMNPs. (b) UV−vis spectra of free Ce6 and FMCNPs. (c) Ce6 loading efficiency and (d) encapsulation efficiency of FMCNPs under different concentrations of added Mn^{2+} and Ce6.

the intracellular active GSH level can be decreased owing to the generation of GSH/Mn^{2+} complexes, which facilitate ROS production. With these features, the FMCNPs show improved antitumor PDT efficacy *in vitro* and *in vivo*. In addition, the Mn^{2+} released into the tumor tissue will be rebonded with a biological chelating agent (*e.g.*, GSH), enabling long-term MRI observations and facilitating the clinical evaluations. Therefore, this work presents a self-assembled multicomponent nanoplatform that not only integrates therapeutics and diagnostics but also allows modulation of the responsive release behavior to offer additional information for cancer therapy, thus providing an alternative theranostic method.

RESULTS AND DISCUSSION

Synthesis and Characterization of FMCNPs. An opalescent colloidal suspension appeared upon mixing a solution of Fmoc-L-L (2 mg mL^{-1}) and Mn^{2+} (0.11 mg mL^{-1}) (Figure 1a, inset). The transmission electron microscopy (TEM) image shows spherical FMNPs with an average diameter of approximately 100 nm (Figure 1a), which is consistent with the dynamic light scattering (DLS) measurements (Figure 1c). The NPs had a ζ-potential of −17 mV, which can be ascribed to deprotonation of the carboxyl groups of Fmoc-L-L, rendering the particle surface negatively charged. More importantly, hydrophobic drugs, such as Ce6, can be readily incorporated into the NPs during the self-assembly

DOI: 10.1021/acsnano.8b03529
ACS Nano 2018, 12, 8266−8276

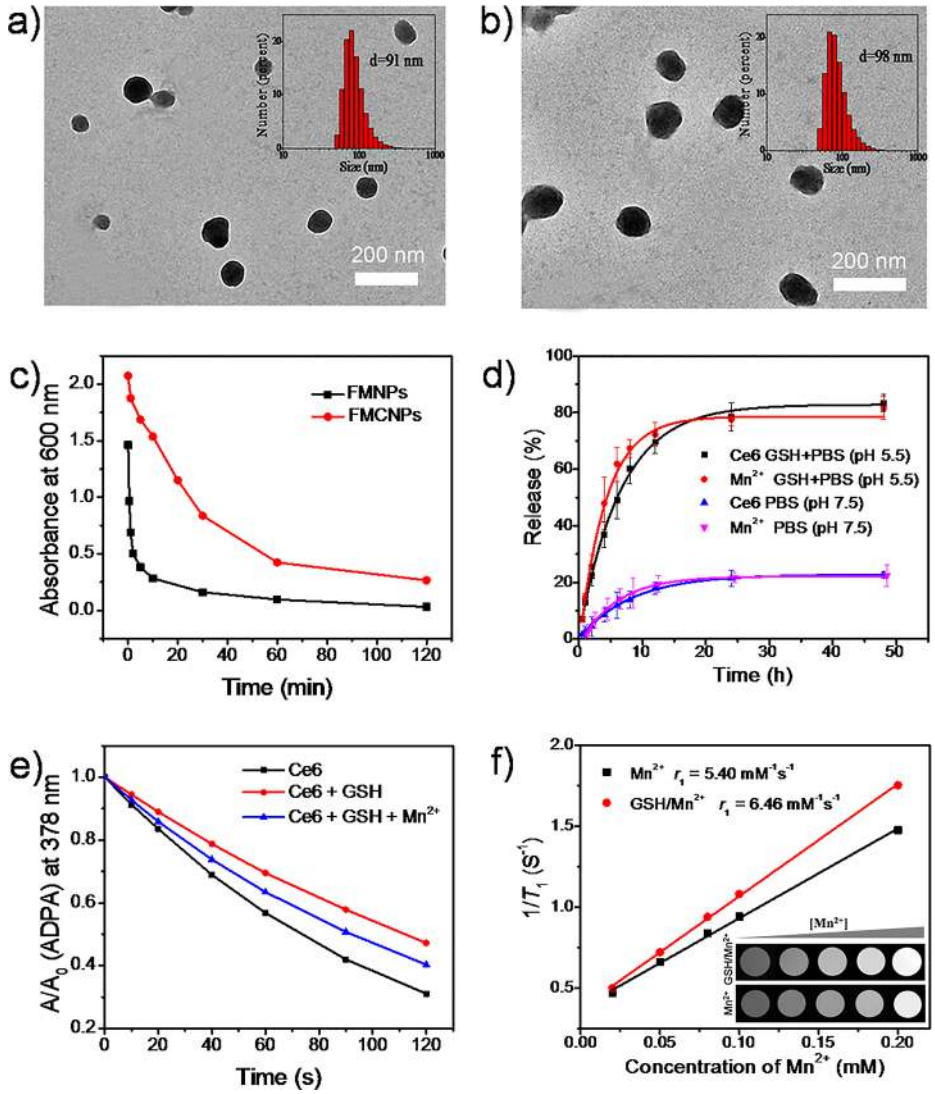

Figure 3. TEM images of the FMCNPs after (a) 8-fold dilution and (b) incubation with 10% (v/v) bovine serum albumin for 24 h. The insets are corresponding size distributions of the samples. (c) Change in the turbidity (absorbance at 600 nm) of FMNP and FMCNP solutions after the addition of GSH. (d) Time-dependent release profiles of Ce6 and Mn^{2+} from FMCNPs as measured by the dialysis method at 37 °C. (e) ROS generation of pure Ce6, Ce6 with GSH, and Ce6 with GSH and Mn^{2+}. (f) T_1 relaxation rate of Mn^{2+} and GSH/Mn^{2+} complexes. The GSH concentration was fixed at 10 mM, and the Mn^{2+} concentration was 0.02, 0.05, 0.08, 0.1, and 0.2 mM. The insets are corresponding T_1 MR images.

process. The addition of an aqueous solution of Mn^{2+} (0.11 mg mL^{-1}) to a mixed solution of Fmoc-L-L (2 mg mL^{-1}) and Ce6 (0.6 mg mL^{-1}) yielded a dark-green turbid suspension (Figure 1b, inset), suggesting that Ce6 was entrapped by the FMNPs to generate FMCNPs. After the integration of Ce6, where the FMCNPs showed a negligible change in morphology, a smaller size was observed (Figure 1b,d), as well as a more negative ζ-potential of −25 mV. The introduction of Ce6 can enhance the hydrophobic interactions with Fmoc-L-L to some extent, shrinking the molecular stacking networks and thus decreasing the particle size. The change in ζ-potential may be attributed to the presence of more carboxylate ($-COO^-$) groups due to the deprotonation of Ce6 carboxyl groups. In the resulting FMCNPs, the loading percentage of Fmoc-L-L, Mn^{2+}, and Ce6 was quantified using a calibration curve constructed from high performance liquid chromatography (HPLC), ion-coupled plasma (ICP), and UV−vis measurement, respectively (Table S1 and Figure S2).

Fourier transform infrared spectroscopy (FTIR) of the FMNPs showed characteristic peaks at 1593 and 1414 cm^{-1}, related to the asymmetrical and symmetrical vibrations of $-COO^-$ groups (Figure 2a), indicating that the $-COO^-$ of the leucine moieties had coordinated with Mn^{2+}.[58] It should be noted that the hydrophobic interactions among Fmoc groups also contribute to the formation of FMNPs, and that they may restrict hydrogen bonds to generate amorphous networks. Compared with the monomeric Ce6, Ce6 in the FMCNPs showed weakened red-shifted absorbance peaks in both the Soret and Q bands (Figure 2b), suggesting the formation of J-aggregates but with defects.[59−62] This presumably contributes to the π-stacking and hydrophobic interactions between the porphin rings of Ce6 and the Fmoc groups of the amino acids.

By adjusting the amount of added Ce6 and Mn^{2+}, the Ce6 loading efficiency can be flexibly tailored, reaching up to *ca.* 36 wt % and an encapsulation efficiency of *ca.* 80% (Figure 2c,d). These data demonstrate the adaptive nature of the coordinated

DOI: 10.1021/acsnano.8b03529
ACS Nano 2018, 12, 8266−8276

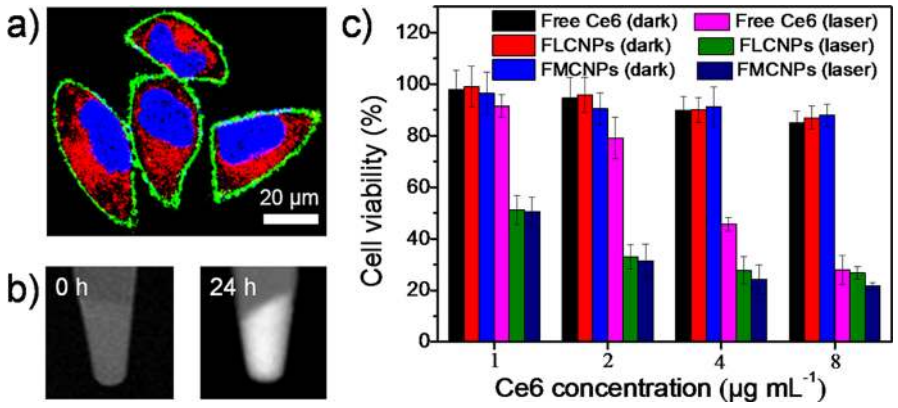

Figure 4. (a) CLSM image of MCF7 cells after incubation with FMCNPs at 37 °C for 24 h. Blue and green fluorescence indicate the cell nucleus and membrane, respectively. (b) *In vitro* T_1-weighted MR images of MCF7 cells collected by centrifugation. (c) MCF7 cell viability after incubation with FLCNPs, FMCNPs, and free Ce6 at various concentrations with and without 660 nm laser irradiation (100 mW cm^{-2}, 1 min).

networks in the FMNPs and the efficiency of this approach for hydrophobic drug delivery. Importantly, the size of the assembled NPs can be flexibly tuned by changing the initial concentration of Fmoc-L-L. The NP size changed from ∼38 to ∼126 nm when the concentration of Fmoc-L-L was altered from 0.5 to 3.0 mg mL^{-1} with a fixed ratio of all the components (Figure S3). In addition, the type of amino acids can be extended to others, such as Fmoc-L-histidine, Fmoc-L-proline, and Fmoc-L-tryptophan for the formation of well-defined NPs (Figures S1 and S4), indicating that amphiphilic amino-acid-coordinated self-assembly is a general strategy for the fabrication of functional NPs capable of drug encapsulation.

Stability and Responsive Release of FMCNPs. For further biomedical applications, the stability of NPs is a priority. The FMCNPs maintained their structural integrality after 8-fold dilution (Figure 3a) and incubation with a solution containing fetal bovine serum (FBS) for 24 h (Figure 3b), confirming their excellent colloidal stability. The robust structure of the NPs is likely the result of the multiple cooperative intermolecular interactions. After FMNPs or FMCNPs were mixed with GSH, the turbidity of the solutions dramatically decreased (Figure 3c), which is indicative of their disassembly in response to GSH. GSH has two carboxyl groups and one thiol group, which chelates various metal ions.[63] Therefore, we suggest that the competitive coordination with Mn^{2+} induced by GSH causes disassembly of the FMCNPs, facilitating the release of Ce6 and Mn^{2+}.

The release of Ce6 and Mn^{2+} from the FMCNPs was further evaluated by dialysis against phosphate-buffered saline (PBS; 10 mM, pH 7.5 and 5.5) in the presence of GSH (10 mM) to simulate the ambient physiology of blood and tumor cells, respectively. Only *ca.* 21% of the Ce6 and Mn^{2+} was released at 48 h in the PBS (Figure 3d), which is consistent with the fact that the FMCNPs are stable against dilution. In contrast, progressive release of the two components was observed when GSH was added to the solution, amounting to *ca.* 80% during the first 15 h (Figure 3d). These release profiles suggest desirable delivery for active reagents, with minimal release in the circulation and accelerated release within tumor cells. The binding of Mn^{2+} with GSH may accelerate the transmembrane transport of Mn^{2+} due to a shift in the thermodynamic equilibrium, as demonstrated by its increased release rate compared to that with free Ce6 (Figure 3d). To further demonstrate the GSH-responsiveness of the FMCNPs, non-responsive nanoparticles (FLCNPs) were prepared as controls using amphiphilic Fmoc-L-Lysine to modulate the interactions with Ce6 following a previously reported method.[52] The resulting NPs were an average of 98 nm in size and had a negative ζ-potential (−18 mV), similar to the FMCNPs (Figure S6). Ce6 has the same release profiles from the FLCNPs in the presence and absence of GSH (Figure S7), confirming that the competitive binding between GSH and Mn^{2+} is the basis of the triggered disassembly of the FMCNPs and the subsequent release of Ce6.

***In Vitro* ROS Generation and MRI.** Considering that GSH can bind with Mn^{2+}, the potential effect of Mn^{2+} on the ROS generation of Ce6 in the presence of GSH was investigated using anthracene-9,10-dipropionic acid (ADPA) as an ROS probe. GSH, as a reducing agent, could in principle consume the ROS generated by Ce6 (Figure 3e) and thus reduce the efficacy of PDT. Interestingly, the addition of Mn^{2+} alleviated the inhibitory effect induced by GSH (Figure 3e), presumably because GSH/Mn^{2+} complexes are less reactive than free GSH. Likewise, we observed that the ROS generation capacity of the FMCNPs in the presence of GSH was significantly greater than that in the absence of GSH (Figure S8). This result indicates that the assembled FMCNPs are apt to disassemble in response to GSH and completely release Ce6. Moreover, the coordination between Mn^{2+} and GSH can inactivate GSH, thus reducing its effect on ROS generation. These characteristics are very favorable for efficient PDT.

Due to the GSH-responsive nature of the FMCNPs, their MRI properties were investigated in the form of GSH/Mn^{2+}. The GSH/Mn^{2+} complex exhibited a superparamagnetic property with an r_1 value of 6.46 mM^{-1} s^{-1} (Figure 3f). *In vitro* MRI examination of GSH/Mn^{2+} showed enhanced T_1-weighted contrast compared to free Mn^{2+} (Figure 3f, inset), which may be ascribed to the increased water exchange rate and reduced molecular tumbling time of GSH/Mn^{2+} complex compared with Mn^{2+}.[64] In this sense, the rechelated Mn^{2+} in the form of GSH/Mn^{2+} has enhanced MRI properties, as demonstrated by the above *in vitro* measurements.

Cellular Uptake and Efficacy of FMCNPs in MCF7 Cancer Cell PDT. The promising data obtained with FMCNPs prompted us to evaluate the dynamic process at the cellular level. Confocal laser scanning microscopy (CLSM) examination of MCF7 breast cancer cells incubated with

DOI: 10.1021/acsnano.8b03529
ACS Nano 2018, 12, 8266−8276

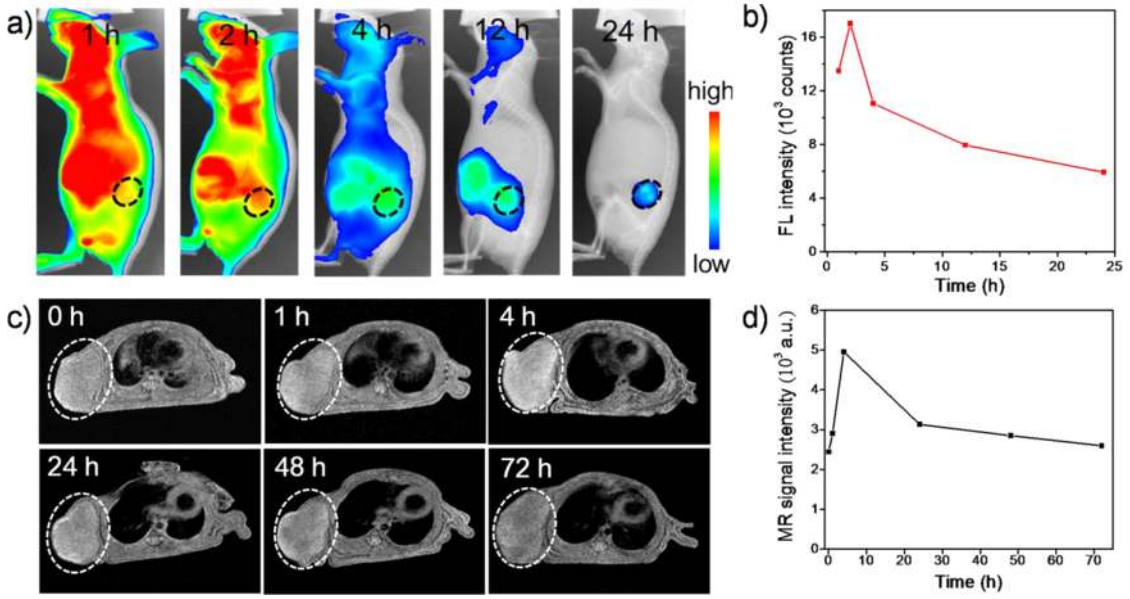

Figure 5. Representative *in vivo* (a) fluorescence images and (c) T_1-weighted MR images of nude mice bearing MCF7 breast cancer xenografts following the intravenous injection of FMCNPs. The dashed circles include the tumor site. (b,d) Variation in the fluorescence and MR signal intensity in (a) and (c), respectively.

FMCNPs showed the uniform dispersion of the red fluorescence of Ce6 in the cytoplasm (Figure 4a), revealing that FMCNPs are internalized by endocytosis and then disassembled in endocytic compartments, such as lysosomes. Compared to free Ce6, FMCNP-treated cells exhibited brighter fluorescence (Figure S9), indicating the superior cellular uptake of the NPs. The intracellular accumulation of Mn^{2+} was monitored by MRI. T_1-weighted MRI showed brighter images with excellent contrast at 24 h, which was ascribed to the paramagnetic Mn^{2+} (Figure 4b). In addition, the MRI intensity increased during the incubation (Figure S10), which is in agreement with the fluorescence observations (Figure S9). These results demonstrate that the continuous uptake of FMCNPs is followed by disassembly induced by GSH in cancer cells. Therefore, the assembled FMCNPs can release their cargo within tumor cells.

Encouraged by the *in vitro* and *in vivo* data that revealed well-controlled Ce6 release in response to the tumor microenvironment, we used FMCNPs for antitumor PDT. Methyl thiazolyl tetrazolium (MTT) assay showed that the FMCNPs have a phototoxicity greater than that of free Ce6, with a median lethal dose 4 times lower than that of free Ce6 (Figure 4c), which is the result of the enhanced cellular uptake (Figure S9). The cytotoxicity of the FLCNPs with and without irradiation was also evaluated and compared to that of the FMCNPs (Figure 4c). No obvious cytotoxicity was observed for the FMCNPs or FLCNPs without irradiation even at the highest tested dose (Figure 4c), suggesting their inherent biocompatibility. In addition, the FLCNPs exhibited less photocytotoxicity than the FMCNPs, especially at higher doses. Moreover, the intracellular ROS production was detected by 2′,7′-dichlorofluorescein diacetate (DCFH-DA) which can be oxidized by ROS to fluorescent 2,7-dichlorofluorescein (DCF) (Figure S11). The FMCNP-treated cells exhibited a fluorescence intensity stronger than that of the FLCNPs. Taken together, these results demonstrate that the FMCNPs can inactivate GSH in MCF7 cancer cells, leading to enhanced ROS generation and PDT efficacy.

Biodistribution and MRI. The *in vivo* distribution of the FMCNPs was further investigated in MCF7 tumor-bearing mice. At 2 h after the injection of the FMCNPs, the fluorescence intensity of the tumor site showed an obvious increase (Figure 5a), suggesting the accumulation of the FMCNPs and release of Ce6 at the tumor site. The fluorescence weakened due to metabolic clearance but remained stronger than that in mice treated with free Ce6 (Figure 5a,b and Figure S12a), showing that the FMCNPs can efficiently deliver Ce6 to tumors, which is a prerequisite for PDT. *Ex vivo* imaging at 24 h postinjection also confirmed that the FMCNPs were capable of improving the bioavailability of Ce6 to favor tumor selectivity (Figure S12b) arising from the enhanced permeability and retention (EPR) effect.[65] Simultaneously, MRI signals were detected in the tumor tissue at 1 h postinjection and reached a maximum after 4 h (Figure 5c,d). This increase is consistent with the change in fluorescence intensity during the early period after injection, further demonstrating the accumulation of FMCNPs in the tumor. Interestingly, the MRI signals were sustained for at least 72 h (Figure 5d), during which time the fluorescence completely disappeared (Figure S12c). This disparity suggests the long-term retention of Mn^{2+} released from the FMCNPs, facilitated by the high affinity of Mn^{2+} for intracellular GSH.[15] During this time, the tumor border can still be distinguished, even at 72 h (Figure 5c), which can provide valuable information for planning and guiding therapeutic actions.

***In Vivo* PDT Studies.** The PDT effects were further evaluated in MCF7 tumor-bearing mice. In the mice treated with FMCNPs, the tumors were successfully suppressed and ablated once applied to laser irradiation (660 nm, 200 mW cm^{-2}, 10 min); however, only a gentle inhibition of tumor growth was observed in mice treated with free Ce6 compared with the control (Figure 6a and Figure S13). Histological analysis by hematoxylin and eosin (H&E) staining showed no tumor cells in the skin at the FMCNP-treated tumor site (Figure 6c). The apoptosis rates of tumors in the Ce6-treated and control groups were further quantified by TUNEL

DOI: 10.1021/acsnano.8b03529
ACS Nano 2018, 12, 8266−8276

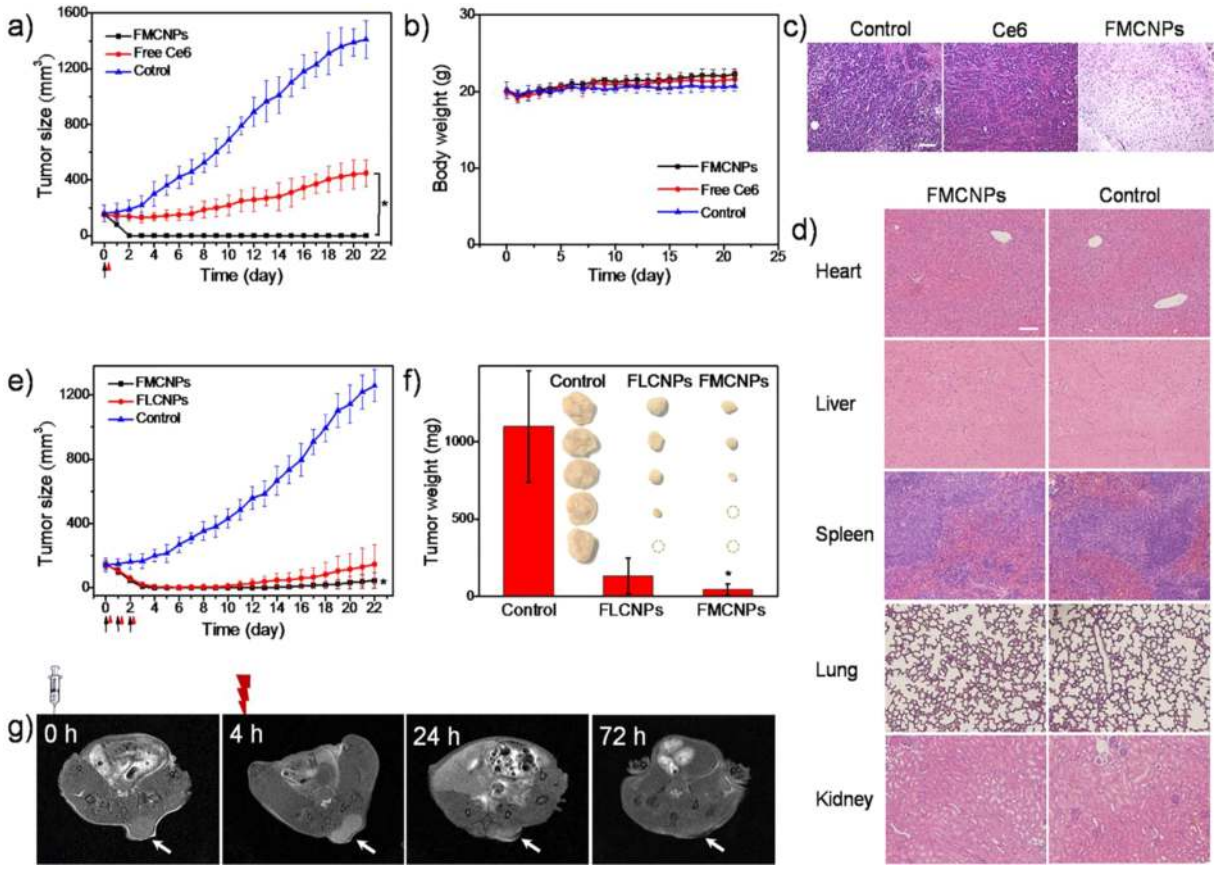

Figure 6. (a) Change in tumor volume of mice bearing MCF7 breast cancer xenografts treated with FMCNPs and free Ce6 (equivalent Ce6 concentration, 5.0 mg kg^{-1} body) followed by irradiation (660 nm, 200 mW cm^{-2}, 10 min). The results are expressed as the mean ± SD. *P < 0.05, one-way ANOVA. (b) Variation in the body weight of MCF7 tumor-bearing mice after various treatments. Representative micrographs from H&E analysis of (c) tumor or hypoderm and (d) major organs from different groups of mice. Scale bars are all 100 μm. (e) Tumor growth inhibition curves of the MCF7 tumor-bearing mice administered FLCNPs and FMCNPs (equivalent Ce6 concentration, 5.0 mg kg^{-1} body weight) on days 0, 1, and 2 (black arrow) followed by irradiation (660 nm, 100 mW cm^{-2}, 10 min) at 4 h postinjection (red arrow). (f) Weights of resected tumors after different treatments (insets: photographs of the tumors). (g) MRI-guided PDT: representative MR images of a mouse administered FMCNPs before and after laser irradiation. White arrows indicate the tumor sites. Images were collected at 0 (preinjection), 4 (irradiation), 24, and 72 h postinjection from the same mouse.

staining. The control group showed negligible apoptosis, with an apoptotic rate of nearly 2%, whereas the apoptotic rate of the free Ce6-treated group was approximately 47% (Figure S14). These results suggest that FMCNPs achieve efficient drug delivery. The body weight and tissue sections of the mice showed no obvious change during the treatments (Figure 6b,d), indicating the safety of FMCNP-based PDT. To reveal the GSH-responsiveness of the coordination platform in PDT, the therapeutic results of the FMCNPs and FLCNPs were compared at reduced irradiation doses but an increased treatment frequency. Both groups showed delayed tumor growth initially, but the tumors treated with FLCNPs showed quicker recurrence and were heavier than tumors treated with FMCNPs (Figure 6e,f). In the three groups, obvious apoptosis was observed in the tumor sections of mice administered FMCNPs, along with infiltrating tumor cells with highly pleomorphic nuclei and many mitotic cells (Figure S15a–c). Moreover, no tumor cells appeared among the infiltrating inflammatory cells at the site of the original tumor in FMCNP-treated mice (Figure S15d). The above results suggest that, in response to GSH, FMCNPs can improve the PDT efficacy *in vivo*. Therefore, FMCNPs have potential as a biocompatible and efficient phototherapy agent.

MRI-Guided PDT. After accumulating in tumor tissue, FMCNPs can induce a tumor-cell-killing effect and enable prolonged MRI observations, effectively integrating two functionalities in a spatiotemporal manner. As a proof of concept, we used MRI to observe tumor growth in MCF7 breast cancer mouse models after the administration of FMCNPs and PDT by laser irradiation. The MR images showed significant FMCNP accumulation at the tumor site at 4 h postinjection (Figure 6g). Tumor shrinkage and an increased necrotic volume at the tumor site were observed at 24 h postinjection (20 h after irradiation) (Figure 6g). MRI also showed almost complete tumor elimination at 3 days postinjection (Figure 6g). Thus, FMCNPs can serve as a theranostic nanoplatform for MRI-guided PDT.

CONCLUSIONS

In summary, we demonstrate the development of a minimalist supramolecular multifunctional theranostic nanoplatform based on amphiphilic amino-acid-coordinated self-assembly. The assembled biometal–organic NPs exhibit multifold advantages for theranostic applications: (1) a facile but green and universal approach; (2) intrinsic biocompatible materials with high biosafety; (3) strong ability to chelate imaging agents

DOI: 10.1021/acsnano.8b03529
ACS Nano 2018, 12, 8266–8276

(Mn^{2+}) and flexible responsiveness to GSH; (4) a one-step process for high drug loading with excellent encapsulation efficiency; and (5) tunable and suitable particle sizes for efficient tumor EPR effect. The nanoplatform enables enhanced cellular uptake and tumor accumulation accompanied by the tumor microenvironment (GSH)-responsive release of drugs and imaging agents, resulting in a superior antitumor efficacy and imaging capability. The binding of GSH with Mn^{2+} gives rise to emerging advantages, including alleviating the inhibition of GSH by ROS production and enhancing the retention time of Mn^{2+} in the tumor. In addition to achieving and validating the nanoscale integration of imaging (MRI) and therapeutic (PDT) functions, the benefits of such a combination allow the real-time monitoring of the *in vivo* delivery of NPs and the noninvasive assessment of the therapeutic efficacy. This integrated platform shows great promise as a highly versatile theranostic agent for cancer. This study also suggests that amino acid or peptide-tuned multicomponent synergetic self-assembly is a promising approach for developing "all-in-one" nanomedicines with improved diagnostic precision and therapeutic efficacy.

EXPERIMENTAL SECTION

Materials. Amphiphilic amino acid Fmoc-L-leucine, Fmoc-L-histidine, Fmoc-L-tryptophan, Fmoc-L-proline, and Fmoc-L-lysine were purchased from Bachem (Bubendorf, Switzerland), and Chlorin e6 was obtained from Frontier Scientific (Newark, Delaware, USA). Other chemicals were purchased from Sigma-Aldrich (St. Louis, Missouri, USA) and used as received unless otherwise stated.

Fabrication of the Drug-Loaded NPs. Typically, 10 mg of Fmoc-L-L powder was dissolved in 300 μL of NaOH solution (0.1 M, pH 13) and then diluted to a final concentration of 10 mg mL^{-1} with ultrapure water. Ce6 (6 mg), the hydrophobic drug, was dissolved in 100 μL of NaOH solution (1 M, pH 14). A $MnCl_2$ aqueous solution (10 mM, 200 μL) was first mixed with 590 μL of ultrapure water; next, the solution was added to the mixture of the above Fmoc-L-L solution (200 μL) and Ce6 solution (10 μL) with the total volume reaching 1 mL. Turbidity appeared immediately when the pH was adjusted to 8.0 by 1 M HCl. The final concentration of Fmoc-L-L, Mn^{2+}, and Ce6 was 2, 0.11, and 0.6 mg mL^{-1}, respectively. To adjust the particle size and drug loading efficiency, different volumes of components were added while the final volume and pH remained fixed. FLCNPs were fabricated according to previously reported work.[52]

Characterizations of FMCNPs. For the size distribution and ζ-potential measurements, a DLS instrument (Nano ZS ZEN3600, Malvern) was used. The TEM image was collected by a JEOL JEM-100 CXII (Japan) at an accelerating voltage of 80 kV on the sample-deposited carbon-coated copper grids. The scanning electron microscopy image was measured on an S-4800 HITACHI (Japan) with clean silica wafers. The absorbance and the fluorescence signals were monitored using a Shimadzu UV-2600 spectrophotometer and Hitachi F-4500 fluorescence spectrometry. VERTEX-70/70v spectrometer (Bruker Optics, Germany) was used to execute FTIR measurement. The sample was centrifuged on an Optima XE supercentrifuge (Beckman Coulter, America). HPLC spectra were performed on a VWD-3100 detector (Thermo Fisher U3000 HPLC system) using an Acclaim 120 C18 HPLC column (Thermo Scientific) at 25 °C. The elemental analysis was performed by ion-coupled plasma mass spectrometry (ICP-MS) on an Agilent 7700 ICP-MS under vacuum. A 660 nm laser (K660E02MN, BWT Beijing LTD, China) was used for irradiation.

Determination of Ingredient Content in FMCNPs. The sample was centrifuged at 50000 rpm for 1 h in a 2 mL centrifuge tube (Beckman Coulter, America). The upper phase was collected for DLS measurements to ensure complete separation. The solids were dissolved in dimethyl sulfoxide (DMSO) and subjected to UV−vis measurements using a quartz cell (1 mm) to quantify the Ce6 content. The particles collected from 1 mL of solution were dissolved in 1 mL of DMSO and then diluted 100 times before measurement. The concentration of assembled Ce6 was calculated using the standard curve for Ce6 (1−30 μg mL^{-1}) in DMSO. HPLC was employed to quantify the content of Fmoc-L-L in the particles using the standard curve of Fmoc-L-L (5−100 μg mL^{-1}) in methanol. Solvent A was water and 0.1% v/v trifluoroacetic acid (TFA), and solvent B was methanol and 0.1% v/v TFA. Fmoc-L-L with a retention time of 17.4 min was monitored at an absorption wavelength of 220 nm with a gradient of solvent B from 60 to 95% over 45 min at a flow rate of 1.0 mL min^{-1}. The amount of Mn^{2+} loaded in the NPs was measured by ICP-MS using the standard curve for Mn^{2+} (2−40 μg L^{-1}) in 1% HNO_3. The Mn^{2+} in the assembled particles in a 1 mL sample was digested in 1% HNO_3, and the final concentration was diluted to less than 100 μg L^{-1} using 1% HNO_3. The loading efficiency and encapsulation efficiency were calculated as follows: loading efficiency (%) = $m_2/m_0 \times 100\%$ (1); encapsulation efficiency (%) = $m_2/m_1 \times 100\%$ (2), where m_2 is the weight of the component in the NPs, m_1 is the weight of the component added to the system, and m_0 is the total weight of the assembled NPs.

Stability Testing. The resuspended FMCNPs were diluted eight times using PBS to observe their stability. The stability was further studied in 10% (v/v) FBS at physiological temperature (37 °C). The treated samples were incubated for 24 h before DLS and TEM measurements.

GSH-Responsive Release of Model Drugs. The Ce6 release profiles *in vitro* were measured by the dialysis method. FMCNPs from a 2 mL sample were collected by centrifugation and redispersed in 1 mL of water. The redispersed solution was pipetted into a dialysis membrane (MW cutoff = 3 kDa) and then dialyzed against 40 mL of PBS solution containing 0.1% (v/v) Tween 80 and 0 mM (pH 7.5) or 10 mM GSH (pH 5.5) in the dark. Next, 1 mL of the dialysate was collected and replaced with 1 mL of fresh medium at the indicated time points. The dynamic change process was monitored by UV−vis spectrophotometry.

Generation and Detection of ROS. ADPA was employed to determine the ROS generation efficiency of Ce6 (5 μg mL^{-1}; 5 μg mL^{-1} containing 1 mM of GSH; and 5 μg mL^{-1} containing 1 mM of GSH and 1 mM of Mn^{2+}). Next, 0.1 mL of ADPA (1 mg mL^{-1}) was mixed with 2.9 mL of the above samples, followed by irradiation with a 660 nm laser. The decrease in the adsorption at 378 nm upon the reaction of ADPA with ROS was measured by UV−vis spectrophotometry. To confirm the active ROS generation, 0.5 mL of ADPA (1 mg mL^{-1}) was added to 2.5 mL of FMCNPs (containing 0.1 mg mL^{-1} of Ce6) in the presence and absence of GSH (10 mM), respectively. The above solutions were incubated for 10 min before laser irradiation.

***In Vitro* Cell Uptake.** Breast cancer cells (MCF7) were seeded in a cover glass chamber at a density of 1×10^6 cells $well^{-1}$ and cultured in Dulbecco's modified Eagle medium (DMEM; Mediatech) supplemented with 10% premium FBS (Gibco) and 1% penicillin−streptomycin (Gibco) in a 5% CO_2 incubator at 37 °C. After 24 h of incubation, the medium was removed, and the cells were washed with PBS gently three times. Then the cells were treated with 2 mL of culture medium containing Ce6-loaded NPs or free Ce6 (10 μg mL^{-1} Ce6). The intracellular delivery of Ce6 was observed by CLSM (Olympus FV1000, Ex = 633 nm) after thorough washing at different time intervals. Hoechst 33342 (1 mg mL^{-1}) staining was performed according to the manufacturer's protocols; 5 μL of Hoechst 33342 was added and allowed to stand for 10 min to stain nuclei. Next, 5 μL of Alexa 488 (1 mg mL^{-1}) was added to the cells and allowed to stand for 10 min. The fluorescence signals were then observed using 405 and 488 nm lasers.

***In Vitro* MTT Assay.** The cytotoxicity of assembled and free Ce6 to MCF7 cells was evaluated by MTT assay. MCF7 cells (1×10^4 cells $well^{-1}$) were seeded in 96-well plates and treated with equal amounts of assembled or free Ce6 at a range of concentrations. The cells were allowed to attach for 24 h before being irradiated by a 660 nm laser (100 mW cm^{-2}) for 1 min. Subsequently, 10 μL of MTT (5

DOI: 10.1021/acsnano.8b03529
ACS Nano 2018, 12, 8266−8276

mg mL^{-1}) solution was added to each well as the color changed to purple-blue. Finally, 100 μL of DMSO was pipetted into the medium, followed by absorbance measurements on a microplate reader (Thermo Fisher Scientific). Cell viability was defined as the percentage of live cells per total control cells. The dark toxicity was evaluated similarly but with no exposure to laser irradiation.

Intracellular ROS Detection. MCF7 cells were cultured in media containing FMCNPs or FLCNPs (equivalent Ce6 concentration, 15 μg mL^{-1}) for 12 h; next, the medium was removed and replaced with DCFH-DA (ROS indicator) dissolved in DMEM (final concentration, 10 μM). After incubation for another 20 min, the cells were exposed to a 633 nm laser (3 mW) for 2 min. The oxidized product DCF (Ex/Em wavelength: 495 nm/529 nm) yielded a fluorescence signal reflecting ROS generation.

Animal Models. The animal experiments complied with animal protection laws of China and were approved by the responsible governmental authority. Female BALB/c-nu mice aged 4–6 weeks were used in the experiments. MCF7 cells (100 μL) at a density of 6 × 10^7 cells mL^{-1} were subcutaneously injected into each mouse. The experiment was conducted until the tumor size reached ~150 mm^3. The tumor volume was calculated according to the following formula: tumor volume = length × $width^2/2$.

MRI. All images were acquired on a 7.0 T Bruker BioSpec system (Bruker BioSpin, Ettlingen, Germany) with a 35 mm quadrature RF transmit and receive coil. Spin echo imaging was performed using a rapid-acquisition relaxation–enhancement sequence with the following parameters: TE, 5.39 ms; TR, 300 ms; rapid acquisition with refocused echoes (RARE) factor, 2; number of excitations, 3; field of view, 40 × 40 mm^2; matrix size, 256 × 256 (in-plane resolution of 0.23 mm); slice thickness, 2 mm for material and 1 mm for cells and mice. The MRI contrast effect of the magnetic NPs at various concentrations (0.02–0.20 mM) was estimated by measuring the proton longitudinal relaxivity, r_1, which was defined as the slope of $1/T_1$ *versus* Mn^{2+} concentration. The T_1-weighted MRI signal intensity was obtained from manually selected image areas. For *in vitro* MRI, MCF7 cells were seeded in culture dishes (10 × 10 cm^2) and cultured with DMEM containing 10% FBS and 1% penicillin/streptomycin until reaching a density of 3 × 10^6 cells per dish. Next, the culture medium was replaced with media containing FMCNPs (equivalent to 60 μmol mL^{-1} Mn^{2+}), and the cells were further incubated for different times. After 2, 8, 12, and 24 h, the medium was discarded, and the cells were washed three times with PBS prior to trypsinization and centrifugation at 800 rpm for 5 min. After the supernatant was discarded, the cell pellets were redispersed with 400 μL of PBS, transferred to small tubes, and centrifuged (800 rpm, 3 min) before MRI. For *in vivo* MRI, the mice bearing tumors on the right shoulder received 200 μL of redispersed of FMCNPs at a dose of 0.2 mmol kg^{-1} Mn^{2+}. For each scan, the mice were anesthetized and placed in a groove-shaped bed inside the scanner (7.4 cm bore) equipped with a birdcage-type RF coil (Rapid Biomedical). The bore was warmed to 37 °C during the experiment. The signal was collected at preset time points. For MRI-guided PDT, the mouse bearing a tumor on the back, the position facilitating irradiation, was 4 weeks old, and their thin body could not fill the groove-shaped bed completely; furthermore, tape was used on the back of the mouse to fix the mouse in the bed; thus, the shape of the longitudinal section slightly varied for each time scan.

Fluorescence Imaging. Equal weights of Ce6 in FMCNPs or as free molecules were intravenously injected into MCF7 tumor-bearing mice before imaging. Fluorescence imaging was performed using an FX Pro system (Carestream Health) with a 670 nm pulsed diode laser and near-infrared fluorescence emission (650–700 nm). The biodistribution was estimated by imaging the mice under anesthesia at designed times. At 24 h postinjection, the heart, liver, lungs, spleen, kidneys, and tumor were excised and imaged, and the fluorescence intensity was acquired using a 12-bit CCD camera (Image Station 4000 mm; Kodak, New Haven, CT) and Kodak MI software (New Haven, CT, USA).

***In Vivo* PDT.** When the tumor volume reached ~150 mm^3, PDT was performed. Tumor-bearing mice (n = 6 for each group) were administered a 5% glucose solution containing FMCNPs or Ce6 molecules at the same concentration (equivalent Ce6 concentration, 5.0 mg kg^{-1} body weight) *via* the tail vein. At 4 h postinjection, the tumor site was irradiated by a 660 nm laser (200 mW cm^{-2}) for 10 min. The control array was treated with 200 μL of saline. The tumor volume and body weight were monitored every day. For histological analysis, tissues were harvested, fixed in 4% paraformaldehyde, embedded in paraffin, and sectioned at 5 μm of thickness. The sections were stained by H&E and observed by optical microscopy. TUNEL staining was performed on tumor sections using a DNA fragmentation detection kit (S7101, Millipore, USA) according to the manufacturer's instructions. The number of apoptotic cells in 10 random fields was counted. The apoptotic rate was calculated as the ratio of the number of apoptotic cells to the total cell number. For comparing the therapeutic efficacy of FMCNPs and FLCNPs, both (equivalent Ce6 concentration, 5.0 mg kg^{-1} body) were injected into the mice (n = 5) at 0, 1, and 2 days; the mice were irradiated by a 660 nm laser (100 mW cm^{-2}, 10 min) at 4 h postinjection. After the mice were sacrificed, the tumors were also collected and weighed.

ASSOCIATED CONTENT

Supporting Information

The Supporting Information is available free of charge on the ACS Publications website at DOI: 10.1021/acsnano.8b03529.

Molecular structures of building blocks; fluorescence spectra of Ce6 in monomeric and assembled forms; SEM images and size distribution of NPs with different amino acids; release profiles of Ce6; confocal images of MCF7 cells incubated with FMCNPs for different times; *in vitro* T_1-weighted MR images of MCF7 cells; *in vivo* fluorescence images; therapeutic results of PDT; components of FMCNPs (PDF)

AUTHOR INFORMATION

Corresponding Authors

*E-mail: xinx@sdu.edu.cn.
*E-mail: shilingyuan@sdu.edu.cn.
*E-mail: yanxh@ipe.ac.cn.

ORCID

Xia Xin: 0000-0002-4886-6028
Shiling Yuan: 0000-0002-4073-9470
Xuehai Yan: 0000-0002-0890-0340

Present Address

[¶]Centre for Systems Chemistry, Stratingh Institute, University of Groningen, 9747 AG Groningen, The Netherlands.

Notes

The authors declare no competing financial interest.

ACKNOWLEDGMENTS

We acknowledge financial support from the National Natural Science Foundation of China (21522307, 21473208, and 91434103), the Talent Fund of the Recruitment Program of Global Youth Experts, and the Key Research Program of the Frontier Sciences of the Chinese Academy of Sciences (QYZDB-SSW-JSC034).

DEDICATION

In the memory of Prof. Helmuth Möhwald.

REFERENCES

(1) Lammers, T.; Aime, S.; Hennink, W. E.; Storm, G.; Kiessling, F. Theranostic Nanomedicine. *Acc. Chem. Res.* **2011**, *44*, 1029–1038.

DOI: 10.1021/acsnano.8b03529
ACS Nano 2018, 12, 8266–8276

(2) Lim, E. K.; Kim, T.; Paik, S.; Haam, S.; Huh, Y. M.; Lee, K. Nanomaterials for Theranostics: Recent Advances and Future Challenges. *Chem. Rev.* **2015**, *115*, 327−394.
(3) Cheng, Z. L.; Al Zaki, A.; Hui, J. Z.; Muzykantov, V. R.; Tsourkas, A. Multifunctional Nanoparticles: Cost *versus* Benefit of Adding Targeting and Imaging Capabilities. *Science* **2012**, *338*, 903−910.
(4) Nguyen, K. T.; Zhao, Y. L. Engineered Hybrid Nanoparticles for On-Demand Diagnostics and Therapeutics. *Acc. Chem. Res.* **2015**, *48*, 3016−3025.
(5) Pelaz, B.; Alexiou, C. H.; Alvarez-Puebla, R. A.; Alves, F.; Andrews, A. M.; Ashraf, S.; Balogh, L. P.; Ballerini, L.; Bestetti, A.; Brendel, C.; Bosi, S.; Carril, M.; Chan, W. C. W.; Chen, C. Y.; Chen, X. D.; Chen, X. Y.; Cheng, Z.; Cui, D. X.; Du, J. Z.; Dullin, C.; et al. Diverse Applications of Nanomedicine. *ACS Nano* **2017**, *11*, 2313−2381.
(6) Gross, S.; Gilead, A.; Scherz, A.; Neeman, M.; Salomon, Y. Monitoring Photodynamic Therapy of Solid Tumors Online by BOLD-Contrast MRI. *Nat. Med.* **2003**, *9*, 1327−1331.
(7) Zou, Q. L.; Abbas, M.; Zhao, L. Y.; Li, S. K.; Shen, G. Z.; Yan, X. H. Biological Photothermal Nanodots Based on Self-Assembly of Peptide Porphyrin Conjugates for Antitumor Therapy. *J. Am. Chem. Soc.* **2017**, *139*, 1921−1927.
(8) Yu, B.; Wei, H.; He, Q. J.; Ferreira, C. A.; Kutyreff, C. J.; Ni, D. L.; Rosenkrans, Z. T.; Cheng, L.; Yu, F. Q.; Engle, J. W.; Lan, X. L.; Cai, W. B. Efficient Uptake of Lu-177-Porphyrin-PEG Nanocomplexes by Tumor Mitochondria for Multimodal-Imaging-Guided Combination Therapy. *Angew. Chem., Int. Ed.* **2018**, *57*, 218−222.
(9) Guo, B.; Sheng, Z. H.; Hu, D. H.; Li, A. R.; Xu, S. D.; Manghnani, P. N.; Liu, C. B.; Guo, L.; Zheng, H. R.; Liu, B. Molecular Engineering of Conjugated Polymers for Biocompatible Organic Nanoparticles with Highly Efficient Photoacoustic and Photothermal Performance in Cancer Theranostics. *ACS Nano* **2017**, *11*, 10124−10134.
(10) Lyu, Y.; Zeng, J. F.; Jiang, Y. Y.; Zhen, X.; Wang, T.; Qiu, S. S.; Lou, X.; Gao, M. Y.; Pu, K. Y. Enhancing Both Biodegradability and Efficacy of Semiconducting Polymer Nanoparticles for Photoacoustic Imaging and Photothermal Therapy. *ACS Nano* **2018**, *12*, 1801−1810.
(11) Smith, B. R.; Gambhir, S. S. Nanomaterials for *In Vivo* Imaging. *Chem. Rev.* **2017**, *117*, 901−986.
(12) Tang, W.; Yang, Z.; Wang, S.; Wang, Z. T.; Song, J. B.; Yu, G. C.; Fan, W. P.; Dai, Y. L.; Wang, J. J.; Shan, L. L.; Niu, G.; Fan, Q. L.; Chen, X. Y. Organic Semiconducting Photoacoustic Nanodroplets for Laser-Activatable Ultrasound Imaging and Combinational Cancer Therapy. *ACS Nano* **2018**, *12*, 2610−2622.
(13) Ehlerding, E. B.; Grodzinski, P.; Cai, W. B.; Liu, C. H. Big Potential from Small Agents: Nanoparticles for Imaging-Based Companion Diagnostics. *ACS Nano* **2018**, *12*, 2106−2121.
(14) Na, H. B.; Lee, J. H.; An, K. J.; Park, Y. I.; Park, M.; Lee, I. S.; Nam, D. H.; Kim, S. T.; Kim, S. H.; Kim, S. W.; Lim, K. H.; Kim, K. S.; Kim, S. O.; Hyeon, T. Development of a T_1 Contrast Agent for Magnetic Resonance Imaging Using MnO Nanoparticles. *Angew. Chem., Int. Ed.* **2007**, *46*, 5397−5401.
(15) Kim, T.; Cho, E. J.; Chae, Y.; Kim, M.; Oh, A.; Jin, J.; Lee, E. S.; Baik, H.; Haam, S.; Suh, J. S.; Huh, Y. M.; Lee, K. Urchin-Shaped Manganese Oxide Nanoparticles as pH-Responsive Activatable T_1 Contrast Agents for Magnetic Resonance Imaging. *Angew. Chem., Int. Ed.* **2011**, *50*, 10589−10593.
(16) Horcajada, P.; Chalati, T.; Serre, C.; Gillet, B.; Sebrie, C.; Baati, T.; Eubank, J. F.; Heurtaux, D.; Clayette, P.; Kreuz, C.; Chang, J. S.; Hwang, Y. K.; Marsaud, V.; Bories, P. N.; Cynober, L.; Gil, S.; Ferey, G.; Couvreur, P.; Gref, R. Porous Metal-Organic-Framework Nanoscale Carriers as a Potential Platform for Drug Delivery and Imaging. *Nat. Mater.* **2010**, *9*, 172−178.
(17) Nel, A.; Xia, T.; Madler, L.; Li, N. Toxic Potential of Materials at the Nanolevel. *Science* **2006**, *311*, 622−627.
(18) Park, Y.; Kim, H. M.; Kim, J. H.; Moon, K. C.; Yoo, B.; Lee, K. T.; Lee, N.; Choi, Y.; Park, W.; Ling, D.; Na, K.; Moon, W. K.; Choi, S. H.; Park, H. S.; Yoon, S. Y.; Suh, Y. D.; Lee, S. H.; Hyeon, T. Theranostic Probe Based on Lanthanide-Doped Nanoparticles for Simultaneous *In Vivo* Dual-Modal Imaging and Photodynamic Therapy. *Adv. Mater.* **2012**, *24*, 5755−5761.
(19) Lee, S. M.; Song, Y.; Hong, B. J.; MacRenaris, K. W.; Mastarone, D. J.; O'Halloran, T. V.; Meade, T. J.; Nguyen, S. T. Modular Polymer-Caged Nanobins as a Theranostic Platform with Enhanced Magnetic Resonance Relaxivity and pH-Responsive Drug Release. *Angew. Chem., Int. Ed.* **2010**, *49*, 9960−9964.
(20) Luk, B. T.; Fang, R. H.; Zhang, L. F. Lipid- and Polymer-Based Nanostructures for Cancer Theranostics. *Theranostics* **2012**, *2*, 1117−1126.
(21) Kono, K.; Nakashima, S.; Kokuryo, D.; Aoki, I.; Shimomoto, H.; Aoshima, S.; Maruyama, K.; Yuba, E.; Kojima, C.; Harada, A.; Ishizaka, Y. Multi-Functional Liposomes Having Temperature-Triggered Release and Magnetic Resonance Imaging for Tumor-Specific Chemotherapy. *Biomaterials* **2011**, *32*, 1387−1395.
(22) Dolmans, D. E. J. G. J.; Fukumura, D.; Jain, R. K. Photodynamic Therapy for Cancer. *Nat. Rev. Cancer* **2003**, *3*, 380−387.
(23) Celli, J. P.; Spring, B. Q.; Rizvi, I.; Evans, C. L.; Samkoe, K. S.; Verma, S.; Pogue, B. W.; Hasan, T. Imaging and Photodynamic Therapy: Mechanisms, Monitoring, and Optimization. *Chem. Rev.* **2010**, *110*, 2795−2838.
(24) Petros, R. A.; DeSimone, J. M. Strategies in the Design of Nanoparticles for Therapeutic Applications. *Nat. Rev. Drug Discovery* **2010**, *9*, 615−627.
(25) Caldorera-Moore, M. E.; Liechty, W. B.; Peppas, N. A. Responsive Theranostic Systems: Integration of Diagnostic Imaging Agents and Responsive Controlled Release Drug Delivery Carriers. *Acc. Chem. Res.* **2011**, *44*, 1061−1070.
(26) Shim, M. S.; Kwon, Y. J. Stimuli-Responsive Polymers and Nanomaterials for Gene Delivery and Imaging Applications. *Adv. Drug Delivery Rev.* **2012**, *64*, 1046−1058.
(27) Liu, D. M.; Poon, C.; Lu, K. D.; He, C. B.; Lin, W. B. Self-Assembled Nanoscale Coordination Polymers with Trigger Release Properties for Effective Anticancer Therapy. *Nat. Commun.* **2014**, *5*, 4182.
(28) Shi, J. J.; Kantoff, P. W.; Wooster, R.; Farokhzad, O. C. Cancer Nanomedicine: Progress, Challenges and Opportunities. *Nat. Rev. Cancer* **2017**, *17*, 20−37.
(29) Schafer, F. Q.; Buettner, G. R. Redox Environment of the Cell as Viewed through the Redox State of the Glutathione Disulfide/Glutathione Couple. *Free Radical Biol. Med.* **2001**, *30*, 1191−1212.
(30) Wei, H.; Zhuo, R. X.; Zhang, X. Z. Design and Development of Polymeric Micelles with Cleavable Links for Intracellular Drug Delivery. *Prog. Polym. Sci.* **2013**, *38*, 503−535.
(31) Wu, J.; Zhao, L. L.; Xu, X. D.; Bertrand, N.; Choi, W. I.; Yameen, B.; Shi, J. J.; Shah, V.; Mulvale, M.; MacLean, J. L.; Farokhzad, O. C. Hydrophobic Cysteine Poly(disulfide)-Based Redox-Hypersensitive Nanoparticle Platform for Cancer Theranostics. *Angew. Chem., Int. Ed.* **2015**, *54*, 9218−9223.
(32) Jiang, F.; Robin, A. M.; Katakowski, M.; Tong, L.; Espiritu, M.; Singh, G.; Chopp, M. Photodynamic Therapy with Photofrin in Combination with Buthionine Sulfoximine (BSO) of Human Glioma in the Nude Rat. *Lasers Med. Sci.* **2003**, *18*, 128−133.
(33) Kiesslich, T.; Plaetzer, K.; Oberdanner, C. B.; Berlanda, J.; Obermair, F. J.; Krammer, B. Differential Effects of Glucose Deprivation on the Cellular Sensitivity towards Photodynamic Treatment-Based Production of Reactive Oxygen Species and Apoptosis-Induction. *FEBS Lett.* **2005**, *579*, 185−190.
(34) Fan, H. H.; Yan, G. B.; Zhao, Z. L.; Hu, X. X.; Zhang, W. H.; Liu, H.; Fu, X. Y.; Fu, T.; Zhang, X. B.; Tan, W. H. A Smart Photosensitizer-Manganese Dioxide Nanosystem for Enhanced Photodynamic Therapy by Reducing Glutathione Levels in Cancer Cells. *Angew. Chem., Int. Ed.* **2016**, *55*, 5477−5482.
(35) Zhang, W.; Lu, J.; Gao, X.; Li, P.; Zhang, W.; Ma, Y.; Wang, H.; Tang, B. Enhanced Photodynamic Therapy by Reduced Levels of

DOI: 10.1021/acsnano.8b03529
ACS Nano 2018, 12, 8266−8276

Intracellular Glutathione Obtained by Employing a Nano-MOF with Cu^{II} as the Active Center. *Angew. Chem.* **2018**, *130*, 4985−4990.
(36) Han, H. S.; Choi, K. Y.; Lee, H.; Lee, M.; An, J. Y.; Shin, S.; Kwon, S.; Lee, D. S.; Park, J. H. Gold-Nanoclustered Hyaluronan Nano-Assemblies for Photothermally Maneuvered Photodynamic Tumor Ablation. *ACS Nano* **2016**, *10*, 10858−10868.
(37) Aida, T.; Meijer, E.; Stupp, S. Functional Supramolecular Polymers. *Science* **2012**, *335*, 813−817.
(38) Rest, C.; Kandanelli, R.; Fernandez, G. Strategies to Create Hierarchical Self-Assembled Structures *via* Cooperative Non-covalent Interactions. *Chem. Soc. Rev.* **2015**, *44*, 2573−2573.
(39) Liu, K.; Zhang, H.; Xing, R. R.; Zou, Q. L.; Yan, X. H. Biomimetic Oxygen-Evolving Photobacteria Based on Amino Acid and Porphyrin Hierarchical Self-Organization. *ACS Nano* **2017**, *11*, 12840−12848.
(40) Sun, Q. H.; Zhou, Z. X.; Qiu, N. S.; Shen, Y. Q. Rational Design of Cancer Nanomedicine: Nanoproperty Integration and Synchronization. *Adv. Mater.* **2017**, *29*, 1606628.
(41) Ariga, K.; Watanabe, S.; Mori, T.; Takeya, J. Soft 2D Nanoarchitectonics. *NPG Asia Mater.* **2018**, *10*, 90−106.
(42) Raymond, D. M.; Nilsson, B. L. Multicomponent Peptide Assemblies. *Chem. Soc. Rev.* **2018**, *47*, 3659−3720.
(43) Northrop, B. H.; Zheng, Y. R.; Chi, K. W.; Stang, P. J. Self-Organization in Coordination-Driven Self-Assembly. *Acc. Chem. Res.* **2009**, *42*, 1554−1563.
(44) Zou, R. F.; Wang, Q.; Wu, J. C.; Wu, J. X.; Schmuck, C.; Tian, H. Peptide Self-Assembly Triggered by Metal Ions. *Chem. Soc. Rev.* **2015**, *44*, 5200−5219.
(45) Zhang, X. J.; Chen, Z. K.; Loh, K. P. Coordination-Assisted Assembly of 1-D Nanostructured Light-Harvesting Antenna. *J. Am. Chem. Soc.* **2009**, *131*, 7210−7211.
(46) Liu, K.; Yuan, C. Q.; Zou, Q. L.; Xie, Z. C.; Yan, X. H. Self-Assembled Zinc/Cystine-Based Chloroplast Mimics Capable of Photoenzymatic Reactions for Sustainable Fuel Synthesis. *Angew. Chem., Int. Ed.* **2017**, *56*, 7876−7880.
(47) Lan, G. X.; Ni, K. Y.; Xu, Z. W.; Veroneau, S. S.; Song, Y.; Lin, W. B. Nanoscale Metal-Organic Framework Overcomes Hypoxia for Photodynamic Therapy Primed Cancer Immunotherapy. *J. Am. Chem. Soc.* **2018**, *140*, 5670−5673.
(48) Fang, Y.; Li, J. L.; Togo, T.; Jin, F. Y.; Xiao, Z. F.; Liu, L. J.; Drake, H.; Lian, X. Z.; Zhou, H. C. Ultra-Small Face-Centered-Cubic Ru Nanoparticles Confined within a Porous Coordination Cage for Dehydrogenation. *Chem.* **2018**, *4*, 555−563.
(49) Nishiyabu, R.; Hashimoto, N.; Cho, T.; Watanabe, K.; Yasunaga, T.; Endo, A.; Kaneko, K.; Niidome, T.; Murata, M.; Adachi, C.; Katayama, Y.; Hashizume, M.; Kimizuka, N. Nanoparticles of Adaptive Supramolecular Networks Self-Assembled from Nucleotides and Lanthanide Ions. *J. Am. Chem. Soc.* **2009**, *131*, 2151−2158.
(50) Imaz, I.; Hernando, J.; Ruiz-Molina, D.; Maspoch, D. Metal-Organic Spheres as Functional Systems for Guest Encapsulation. *Angew. Chem., Int. Ed.* **2009**, *48*, 2325−2329.
(51) Yu, G. C.; Yung, B. C.; Zhou, Z. J.; Mao, Z. W.; Chen, X. Y. Artificial Molecular Machines in Nanotheranostics. *ACS Nano* **2018**, *12*, 7−12.
(52) Liu, K.; Xing, R. R.; Zou, Q. L.; Ma, G. H.; Mohwald, H.; Yan, X. H. Simple Peptide-Tuned Self-Assembly of Photosensitizers towards Anticancer Photodynamic Therapy. *Angew. Chem., Int. Ed.* **2016**, *55*, 3036−3039.
(53) Wojtecki, R. J.; Meador, M. A.; Rowan, S. J. Using the Dynamic Bond to Access Macroscopically Responsive Structurally Dynamic Polymers. *Nat. Mater.* **2011**, *10*, 14−27.
(54) Tao, K.; Levin, A.; Adler-Abramovich, L.; Gazit, E. Fmoc-Modified Amino Acids and Short Peptides: Simple Bio-Inspired Building Blocks for the Fabrication of Functional Materials. *Chem. Soc. Rev.* **2016**, *45*, 3935−3953.
(55) Wang, J.; Liu, K.; Xing, R. R.; Yan, X. H. Peptide Self-Assembly: Thermodynamics and Kinetics. *Chem. Soc. Rev.* **2016**, *45*, 5589−5604.
(56) Zou, Q. L.; Yan, X. H. Amino Acid Coordinated Self-Assembly. *Chem. - Eur. J.* **2018**, *24*, 755−761.
(57) Pan, D. P. J.; Caruthers, S. D.; Senpan, A.; Schmieder, A. H.; Wickline, S. A.; Lanza, G. M. Revisiting an Old Friend: Manganese-Based MRI Contrast Agents. *Wires. Nanomed. Nanobi.* **2011**, *3*, 162−173.
(58) Lama, P.; Sañudo, E. C.; Bharadwaj, P. K. Coordination Polymers of Mn^{2+} and Dy^{3+} Ions Built with a Bent Tricarboxylate: Metamagnetic and Weak Anti-Ferromagnetic Behavior. *Dalton Trans.* **2012**, *41*, 2979−2985.
(59) Verma, S.; Ghosh, A.; Das, A.; Ghosh, H. N. Ultrafast Exciton Dynamics of J- and H-Aggregates of the Porphyrin-Catechol in Aqueous Solution. *J. Phys. Chem. B* **2010**, *114*, 8327−8334.
(60) Okada, S.; Segawa, H. Substituent-Control Exciton in J-aggregates of Protonated Water-Insoluble Porphyrins. *J. Am. Chem. Soc.* **2003**, *125*, 2792−2796.
(61) Wurthner, F.; Kaiser, T. E.; Saha-Moller, C. R. J-Aggregates: From Serendipitous Discovery to Supramolecular Engineering of Functional Dye Materials. *Angew. Chem., Int. Ed.* **2011**, *50*, 3376−3410.
(62) Nam, Y. S.; Shin, T.; Park, H.; Magyar, A. P.; Choi, K.; Fantner, G.; Nelson, K. A.; Belcher, A. M. Virus-Templated Assembly of Porphyrins into Light-Harvesting Nanoantennae. *J. Am. Chem. Soc.* **2010**, *132*, 1462−1463.
(63) Cobbett, C.; Goldsbrough, P. Phytochelatins and Metallothioneins: Roles in Heavy Metal Detoxification and Homeostasis. *Annu. Rev. Plant Biol.* **2002**, *53*, 159−182.
(64) Werner, E. J.; Datta, A.; Jocher, C. J.; Raymond, K. N. High-Relaxivity MRI Contrast Agents: Where Coordination Chemistry Meets Medical Imaging. *Angew. Chem., Int. Ed.* **2008**, *47*, 8568−8580.
(65) Lavik, E.; Von Recum, H. The Role of Nanomaterials in Translational Medicine. *ACS Nano* **2011**, *5*, 3419−3424.

DOI: 10.1021/acsnano.8b03529
ACS Nano 2018, 12, 8266−8276